Theses and Dissertations — 1. Thesis and Dissertation Collection, all items

1994-12

Thickness measurement of ammonia targets used in SLAC E143 experiment

Garvey, David Raymond

Monterey, California. Naval Postgraduate School

http://hdl.handle.net/10945/42803

NAVAL POSTGRADUATE SCHOOL
MONTEREY, CALIFORNIA

THESIS

THICKNESS MEASUREMENT OF
AMMONIA TARGETS USED IN
SLAC E143 EXPERIMENT

by

David Raymond Garvey

December, 1994

Thesis Advisor: Xavier K. Maruyama

REPORT DOCUMENTATION PAGE

Form Approved OMB No. 0704-0188

1. AGENCY USE ONLY *(Leave blank)*	2. REPORT DATE December, 1994	3. REPORT TYPE AND DATES COVERED Master's Thesis

4. TITLE AND SUBTITLE THICKNESS MEASUREMENT OF AMMONIA TARGETS USED IN SLAC E143 EXPERIMENT	5. FUNDING NUMBERS
6. AUTHOR(S) Garvey, David, R.	

7. PERFORMING ORGANIZATION NAME(S) AND ADDRESS(ES) Naval Postgraduate School Monterey, CA 93943	8. PERFORMING ORGANIZATION

9. SPONSORING/MONITORING AGENCY NAME(S) AND ADDRESS(ES)	10. SPONSORING/MONITORING

11. SUPPLEMENTARY NOTES The views expressed in this thesis are those of the author and do not reflect the official policy or position of the Department of Defense or the U.S. Government.

12a. DISTRIBUTION/AVAILABILITY STATEMENT Approved for public release; distribution is unlimited.	12b. DISTRIBUTION CODE

13. ABSTRACT *(maximum 200 words)*

One of the primary research tools in high energy physics is the collision of beams of particles with stationary targets. The useful information that may be extracted from such experiments is proportional to knowledge of the thickness of the target. This determines how many point constituents were available for the particles in the beam to interact with. It is possible to determine the thickness of a target with statistical errors of the order of one percent by the use of x-ray attenuation measurements.

Six target samples from the Stanford Linear Accelerator Center Experiment #143, "Nucleon Spin Structure at 30 GeV," were measured using this method. The targets were frozen ammonia crystals. A 40 mCurie americium 241 source was used to pass a collimated beam of known intensity x-rays through the samples. The x-ray intensity on the other side was measured by a silicon detector. The ammonia material was removed and the process repeated. By comparing the intensities with and without the material to the tabulated attenuation coefficients, the thickness of material is calculated.

14. SUBJECT TERMS radiation attenuation, thickness measurements, dilution factor, packing fraction			15. NUMBER OF PAGES 48
			16. PRICE CODE

17. SECURITY CLASSIFICATION OF REPORT Unclassified	18. SECURITY CLASSIFICATION OF THIS PAGE Unclassified	19. SECURITY CLASSIFICATION OF ABSTRACT Unclassified	20. LIMITATION OF ABSTRACT UL

THICKNESS MEASUREMENT OF AMMONIA
TARGETS USED IN SLAC
E143 EXPERIMENT

by

David R. Garvey
Lieutenant, United States Navy
B.A., University of Washington, 1988

Submitted in partial fulfillment
of the requirements for the degree of

MASTER OF SCIENCE IN PHYSICS

from the

**NAVAL POSTGRADUATE SCHOOL
December 1994**

Author: _____

David R. Garvey

Approved by: _____

Xavier K. Maruyama, Thesis Advisor

Fred R. Buskirk, Second Reader

William B. Colson, Chairman
Department of Physics

iii

Accession For

NTIS GRA&I	☑
DTIC TAB	☐
Unannounced	☐
Justification

By_____

Distribution/

Availability Codes

| Dist | Avail and/or Special |

ABSTRACT

One of the primary research tools in high energy physics is the collision of beams of particles with stationary targets. The useful information that may be extracted from such experiments is proportional to knowledge of the thickness of the target. This determines how many point constituents were available for the particles in the beam to interact with. It is possible to determine the thickness of a target with statistical errors of the order of one percent by the use of x-ray attenuation measurements.

Six target samples from the Stanford Linear Accelerator Center Experiment #143, "Nucleon Spin Structure at 30 GeV," were measured using this method. The targets were frozen ammonia crystals. A 40 mCurie americium 241 source was used to pass a collimated beam of known intensity x-rays through the samples. The x-ray intensity on the other side was measured by a silicon cell detector. The ammonia material was removed and the process repeated. By comparing the intensities with and without the material to the tabulated attenuation coefficients, the thickness of material is calculated.

TABLE OF CONTENTS

LIST OF FIGURES

ACKNOWLEDGMENTS

I would like to thank Professor X.K. Maruyama first and foremost for his patience and personality. In allowing me to join him in representing the Naval Postgraduate School (NPS) during the SLAC "Nucleon Spin Structure at 30 GeV" experiment, I had the opportunity to work with members of the international scientific community whom I otherwise would never have met. Professor Maruyama constantly stressed the real life processes that make implementing an experimental endeavor of this magnitude so difficult. Our relationship was never formal or strained and his friendship was as valuable as his mentorship.

I would also like to thank all the members of the E143 Collaboration who made a Masters Degree candidate feel comfortable working amongst PhD candidates, for dozens of PhD advisors on a project of such magnitude. Their true love of science was best shown during the July meeting when the preliminary results were being flashed across an overhead projector and E143 spokesman Dr. Ray Arnold said, "Hold on a minute, we've waited 25 years for these results, let us look at them for a while."

Professor Fred Buskirk of NPS was of invaluable assistance as Second Reader on my thesis and in particular as my tutor in the theoretical concepts of hadron interactions that were so necessary to be able to interact with the other members of the E143 Collaboration. Professor Buskirk was also part of the NPS team that ran the linac to irradiate ammonia samples for use in E143. Mr. Don Snyder and Mr. Harold Riedtyk are the backbone of all linac operations at NPS and were thus invaluable to the irradiation process. Their knowledge of computer hardware and software were was also of great assistance throughout my involvement in this project.

I would also like to thank my high school physics teacher, Rex Siegfried, to whom I deeply apologize for neglecting my final quarter independant study period with him because of foolish romantic pursuits. I hope that this makes it up to him. Finally, I would like to thank my wife Julienne and my three children James, Kirra and Cameron for putting up with all my hours at the computer late at night, the trips to Stanford for various meetings or experiments and the endless hilighting. Without them, I never could have completed my stay at NPS.

I. INTRODUCTION

Nuclear and particle physics has long been a branch of science that, by necessity, takes an indirect approach. Investigators of the subatomic world developed the approach of accelerating beams of individual charged particles at bulk collections of other particles (targets) to check predictions of theoretical models. In 1911 Ernest Rutherford postulated a dense nucleus at the center of the atom in contrast to the dispersed "Rice Pudding" model of the time, because his scattering experiments sometimes gave large angle scattering events that could only be explained if the positive charge was distributed over a relatively much smaller volume than the radii of the "electron cloud."

To probe smaller distance scales requires beams that transfer larger momentum. This is a consequence of the Heisenberg Uncertainty Principle which states that the product of the root mean square uncertainties in position and momentum is, at best, of the order of Planck's Constant. Therefore, to probe distances ~1fm requires momentum transfers of at least a few hundred MeV/c. By the mid-1960's, the Stanford Linear Accelerator Center in Palo Alto, California was using beams of electrons of such high momentum and energy in their experiments that they began to observe the same large angle scattering from free point-like sources within individual nucleons. These experimental point-like objects were termed "partons" by R.P. Feynman, and later it became accepted that they included the "quarks" of M. Gell-Mann. Over the span of a few years, the theory of hadron interactions evolved from the exchange of Yukawa mesons between iso-spin singlets of SU(2) (nucleons), to the exchange of gluons between color singlets of SU(3)$\otimes$SU(3) (quarks), and quantum chromodynamics was born.

Over two decades later, the theory was faced with what became known as "The Proton Spin Crisis." A QCD calculation known as "The Ellis-Jaffe Sum Rule" predicted that the spin of the nucleon was simply the sum of the spins of the constituent quarks (Ellis, J. and Jaffe, R., 1974). Early attempts to verify the prediction were inconclusive due to relatively large random uncertainties (Alguard, M.J., *et al.*, SLAC E80, 1976 and 1978 and Baum G. *et al.*, SLAC E130, 1983). In 1988, after more precise measurement techniques became available, it was reported by experimenters at CERN that their observation of scattering events did not support the Ellis-Jaffe prediction (Ashman, J., *et al.*, EMC, 1988 and 1989). Over the next six years, collaborations of physicists hurried to repeat this experiment and check the findings both at CERN and SLAC (Abe, K., *et al.*, 1994, Adams, D., *et al.*, SMC, 1994, Adeva, B., *et al.*, SMC, 1993 and Anthony, P.L., *et al.*, E142, 1993).

The most recent of these was the E143 experiment. E143 used polarized electrons of up to 29.1 GeV to bombard a polarized ammonia target. In order to determine the number of protons available for

the beam to interact with, and thus evaluate the desired experimental quantities, it was necessary to determine the thickness of the target. This thesis is the report of the measurement of the E143 target inserts by comparing relative intensity data from the attenuation of ^{241}Am x-rays passing through the target material. The advantage of the E143 setup was that using electrons at SLAC (as opposes to the higher energy muons at CERN) allowed for random beam polarization flips and much higher currents and, consequently, event rates. These two factors allowed for far better experimental statistics in this energy range than ever aceived before (Abe, K., *et al.*, 1994 and McCarthy, J., *et al.*, 1993). In order to preserve the advantage of low experimental error in the experiment overall, the contributions of error from other variables such as beam polarization, target polarization and target thickness had to be minimized. The value of the target thickness needed to be known to better than 3% fractional uncertainty in order to preserve the desired low error of the entire experiment (McCarthy, J., *et al.*, 1993). This thesis is a record of the experimental work that was performed by myself and my advisor from September, 1993 through September, 1994 to precisely and accurately measure the ammonia target thicknesses used in the Stanford Linear Accelerator Center Experiment #143. Reduction of the random uncertainty of this experiment directly contributes to international understanding of what has come to be known as the "Nucleon Spin Crisis."

II. GENERAL THEORETICAL BACKGROUND

The modern theory of the strong interaction between hadrons is called quantum chromodynamics or "QCD." As its name implies the prefix "chromo-" refers to color. In the relativistic quantum field theory required to describe QCD, the quantum "numbers" assigned to the individual constituents are called "color." The individual constituents of QCD theory are called "quarks" and they are held together in the form of hadrons via the color fields mediated by "gluons." This is analogous to the individual constituents of QED (quantum electrodynamics), the electrons, being held together in patterns around the nucleus via the Maxwell fields mediated by photons. There are, however, several critical differences between the well known QED and the newer QCD theories. The color fields of QCD theory are examples of non-Abelian gauge fields while the Maxwell fields of QED are Abelian gauge fields. The difference is that the force mediators, bosons, of an Abelian gauge theory are not influenced by the force they carry, i.e. they do not carry the "charge" of their force. In a non-Abelian gauge field theory, however, the force mediating bosons do feel the strong force and do carry the color charge themselves. This leads to very powerful, non linear self interactions and so the conventional perturbation theory of canonical quantum mechanics is invalid. Two more remarkable results of this decidedly different mathematical description of the strong force are "color confinement" and "asymptotic freedom." Color confinement refers to the fact that all physical bound hadron states are composed of multiple quarks whose net color charge sums to zero, i.e., lone quarks with a "bare" color charge are not observed. Asymptotic freedom means that the closer together quarks are, the less they feel the strong force. In the limit of zero range (requiring infinite energy by the Uncertainty Principle mentioned above), they are "free" particles and feel no strong force at all. One way to explain these two phenomena is to consider the partons/quarks as eigenstates of the free field Hamiltonian and thus only truly realizable in the limit of infinite energy (Feynman, R.P., 1972).

The most enduring model of hadron structure is the "naive" quark-parton model (Bjorken, J.D., 1966 and Feynman, R.P., 1972). In this model, the nucleon is composed of three "constituent" quarks of various "flavors," primarily "up" and "down" for the vast majority of visible matter in the universe. The flavors are quantum numbers of the global SU(3) symmetry of the strong force, while the colors are quantum numbers of the local SU(3) symmetry. The Uncertainty Principle accounts for yet another strange effect. On the sub fermi scale, the "vacuum" in relativistic quantum field theory is constantly creating and annihilating particles and anti-particles with masses (energies) inversely proportional to their lifetimes. This means that the constituent quarks inside of hadrons are also immersed in a "virtual sea" of other particles, primarily "strange" quarks. This constituent quark model has been very successful in describing global hadron properties such as charge and mass so it was assumed that it would work equally well in predicting the spin of the hadron to be the superposition of the spins of the effective fields of the constituent quarks. Surprisingly, this was not the case (Ashman *et al.*, EMC, 1988 and 1989).

A. DEEP INELASTIC E-P SCATTERING

One of the primary modern tools of testing QCD predictions is deep inelastic scattering of leptons by hadrons. There are several reasons that this is such a desirable method of probing nucleon structure. First of all, leptons do not experience the strong force and so the reaction is governed, to first order, by single interaction kinematics. Secondly, since leptons have such small masses, they may be accelerated to an ultra relativistic state by lesser applied forces than those required to produce an equal effect in more massive probes. The calculations are performed in the limit of infinite momentum. What this means is that the state of asymptotic freedom mentioned above is assumed to be in effect. Tests of the electromagnetic structure functions of the nucleon provide insight into the parton distribution inside. The name "deep inelastic," means that a great deal of the incident electron's momentum is transferred to the target nucleon, and so a finer structure may be discerned as discussed in the introduction. Since modern electron beams are in the ultra relativistic regime ($\gamma \sim 10^4$) and nucleon targets are, by definition, at rest in the lab frame of reference, it is convenient to analyze the kinematics in that frame. Figure (1) provides an illustration of the relation between the beam axis, taken to be in the +z direction, and the nucleon, taken to be at rest in the laboratory reference frame.

$p = cp^\mu = (E, cp)$ = electron four-momentum   Final electron state: $|p'\rangle$

Initial electron state: $|p, s\rangle$ Scattering angle: θ

Virtual photon momentum: $|q, \varepsilon\rangle$

Final nucleon states: $\sum_n \langle n|P'\rangle$

Initial nucleon state: $|P, S\rangle$ $P = cP^\mu = (M, 0)$ = nucleon four-momentum

$q^2 = q^\mu q_\mu = -Q^2 = (p^\mu - p'^\mu)^2 = -4EE'\,Sin^2(\theta/2) = -2EE'[1 - Cos(\theta)] \leq 0$

Figure 1. Schematic diagram of polarized deep inelastic electron-nucleon scattering.

Other kinematic variables used to describe the collision interaction are (Bjorken, J.D., 1970 and Bjorken, J.D. and Paschos, E.A., 1969, Feynman, R.P., p. 126, 1972, Hughes, V.W. and Kuti, J., 1983 and Kaku, M., 1993, pp. 460-461):

E = Energy, in GeV, of the incident electron beam in the lab reference frame.

E' = Energy, in GeV, of the scattered electron beam in the lab reference frame.

$m = m_e c^2$ = rest mass energy of the electron ~ 0.51 MeV.

$M = M_p c^2$ = rest mass energy of the nucleon ~ 940 MeV = $(P^\mu Q_\mu)/(E-E')$.

$\nu = E-E' = (P^\mu Q_\mu)/M$ = energy transferred from electron to nucleon by virtual photon.

$\varepsilon = \left\{ 1 + 2\left[1 + \left(\frac{\nu}{Q}\right)^2 \right] \mathrm{Tan}^2\left(\frac{\theta}{2}\right) \right\}^{-1}$ = polarization of virtual photon.

$s = m^{-1}(cp, 0, 0, +/- E)$ = spin polarization four-vector of the electron.

$S = (0, \sigma)$ = spin polarization four-vector of the nucleon.

$\Rightarrow P^2 = P^\mu P_\mu = M^2,\ S^2 = S^\mu S_\mu = -1,\ P^\mu S_\mu = 0.$

B. ELECTROMAGNETIC FORM FACTORS

Even though lepton-hadron scattering is a strictly electromagnetic process at accelerator energies, the strong interaction modifies the hadron electromagnetic current at the sub-fermi size scale. In the "naive" quark/parton model, the interaction is assumed to occur due to hard scattering of a virtual photon off of a single constituent of the nucleon, possessing some positive, real fraction of the total nucleon spin and momentum. The differential cross section for deep inelastic scattering of polarized electrons from polarized nucleons in the first Born approximation, with factors of Planck's constant suppressed, is (Hughes, V.W. and Kuti, J., 1983, Kaku, M., 1993, p. 462 and McCarthy, J., *et al.*, E143, 1993)

$$\frac{d^2\sigma_{pol}}{d\Omega dE'} = \left(\frac{2\alpha}{Q^2}\right)^2\left(\frac{E'}{E}\right)L_{\mu\nu}H^{\mu\nu} = \frac{4\sigma_{Mott}L_{\mu\nu}H^{\mu\nu}}{4EE'+Q^2}. \tag{1}$$

In this equation, $L_{\mu\nu}$ is the charged leptonic tensor amplitude, $H^{\mu\nu}$ is the charged hadronic tensor amplitude, α is the electromagnetic fine structure constant, (E'/E) is the relativistic recoil effect term and σ_{Mott} is the Mott scattering cross section (Bosted, P., 1993),

$$\sigma_{Mott} = \left[\frac{2\alpha E'\mathrm{Cos}\left(\frac{\theta}{2}\right)}{Q^2}\right]^2 = \left[\frac{\alpha\mathrm{Cos}\left(\frac{\theta}{2}\right)}{2E\mathrm{Sin}^2\left(\frac{\theta}{2}\right)}\right]^2. \tag{2}$$

The leptonic tensor amplitude is defined as the contribution of the electron-photon vertex in the Feynman diagram for the scattering process. It may be decomposed into a spin-independent symmetric part and a

5

spin-dependent anti-symmetric portion (Feynman, R.P., p. 126, 1972, Hughes, V.W. and Kuti, J., 1983 and Kaku, M., 1993, p. 462). Summed over final polarization states of the scattered electron, $L_{\mu\nu}$ becomes

$$L_{\mu\nu} = L^{(S)}{}_{\mu\nu} + iL^{(A)}{}_{\mu\nu} = \left(p'_\mu p_\nu + p'_\nu p_\mu - g_{\mu\nu} p^\sigma p'_\sigma\right) + i\left(m\varepsilon_{\mu\nu\alpha\beta} S^\alpha q^\beta\right), \tag{3}$$

where $\varepsilon^{\mu\nu\alpha\beta}$ is the completely anti-symmetric fourth rank tensor, $\varepsilon^{1234}=1$, and $g_{\mu\nu}$ is the Minkowski metric. In a similar fashion, the hadron tensor may also be decomposed into a spin-independent symmetric part and a spin-dependent anti-symmetric portion (Ellis, J. and Jaffe, R., 1974, Feynman, R.P., p. 126, 1972, Hey, A.J.G. and Mandula, J.E., 1972, Hughes, V.W. and Kuti, J., 1983, Kaku, M., 1993, pp. 462, Kuti, J. and Weisskopf, F., 1971 and Pokorski, 1987, p. 176). Written in terms of the expectation value of current operators between initial and final states $H^{\mu\nu}$ becomes

$$H^{\mu\nu} = H_{(S)}{}^{\mu\nu} + iH_{(A)}{}^{\mu\nu} = \sum_i (2\pi)^4 \delta(q + P - P')\langle P,\, S|J^\mu(0,\bar{0})|i\rangle\langle i|J^\nu(0,\bar{0})|P,\, S\rangle$$

$$= \sum_i (2\pi)^4 \delta(q + P - P')\langle UP,\, S|j^\mu(0,\bar{0})U(0)|i\rangle\langle i|U^{-1}(0)j^\nu(0,\bar{0})|UP,\, S\rangle, \tag{4}$$

where J^μ is the fully interacting, Heisenberg picture, hadronic current operator for lepton scattering in the global SU(3) approximation and j^μ is the corresponding Schroedinger picture "free" or "bare" current. It can be shown (Drell, S.D., Levy, D.J. and Yan, T., 1969 and 1970, Feynman, R.P., 1972, Ji, X., 1993, Kaku, M., 1993 and Kuti, J. and Weisskopf, F., 1971) that j^μ is also the sum of a symmetric, conserved, vector part and an anti-symmetric, partially conserved axial part. The sum over 'i' in Equation (4) is over all possible final hadron states. After the summation, the expression for the hadronic tensor amplitude further reduces to (Drell, S.D., Levy, D.J. and Yan, T., 1969 and 1970, Hughes, V.W. and Kuti, J., 1983, Kaku, M., 1993, p. 462 and Pokorski, 1987, p. 175)

$$H^{\mu\nu} = \int d^4x\, e^{iqx}\langle P,\, S|\left[J^\mu(0,\bar{x}), J^\nu(0,\bar{0})\right]|P,\, S\rangle. \tag{5}$$

In this step, the operator product of the currents is converted to a commutator because the two differ by a term proportional to $\delta(q + p - p')$ which is always identically zero in physical situations where q and Δp are always strictly positive (Kaku, M., 1993, pp. 462 and Pokorski, 1987, pp. 175). The commutator may then be evaluated using light cone analysis (Drell, S.D., Levy, D.J. and Yan, T., 1969 and 1970 and Feynman, 1972) to give a theoretical value to compare to.

The spin-independent symmetric part of the hadron tensor may be completely defined by two real scalar spin-independent structure functions, W_1 and W_2. From conserved parity and current arguments, as well as Lorentz and gauge invariance, the symmetric part of the hadronic tensor amplitude must have the general form (Drell, S.D., Levy, D.J. and Yan, T., 1969 and 1970, Feynman, R.P., p. 127, 1972, Hey, A.J.G. and Mandula, J.E., 1972, Jaffe, R.L., 1975, Ji, X., 1993 and Kaku, M., 1993, p. 462)

$$H_{(S)}{}^{\mu\nu} = \left(-g^{\mu\nu} + \frac{q^\mu q^\nu}{q^2}\right)W_1 + \left(\frac{c}{M}\right)^2 \left(P^\mu - q^\mu \frac{P \cdot q}{q^2}\right)\left(P^\nu - q^\nu \frac{P \cdot q}{q^2}\right)W_2$$

$$= \left(\frac{c}{M}\right)^2 \left[P^\mu + P^\alpha \left(\frac{q_\alpha q^\mu}{Q^2}\right)\right]\left[P^\nu + P^\beta \left(\frac{q_\beta q^\nu}{Q^2}\right)\right]W_2 - \left[g^{\mu\nu} + g^{\lambda\nu}\left(\frac{q_\lambda q^\mu}{Q^2}\right)\right]W_1, \quad (6)$$

averaged over initial polarization states of the nucleon. Also note that definitions of structure functions throughout the references differ by factors of M^2/ν used for normalization (Bosted, P., 1993 and Ji, X., 1993). Similarly, an expression for the spin-dependent, anti-symmetric part of the hadronic tensor amplitude may be given in terms of two spin-dependent structure functions, G_1 and G_2 (Hey, A.J.G. and Mandula, J.E., 1972, Hughes, V.W. and Kuti, J., 1983 and Ji, X., 1993) and $H_{(A)}{}^{\mu\nu}$ becomes

$$H_{(A)}{}^{\mu\nu} = \varepsilon^{\mu\nu\alpha\beta} q_\alpha \left\{ M S_\beta G_1 + \frac{1}{M}\left[(P_\lambda q^\lambda)S_\beta - (S_\xi q^\xi)P_\beta\right]G_2 \right\}, \quad (7)$$

1. The Bjorken scaling limit

Bjorken theorized (Bjorken, J.D., 1966 and 1970) that in the scaling limit as ν and Q^2 go to infinity, the structure functions become dependent not on ν and Q^2, but rather on their ratio and the mass of the target nucleon. This ratio became known as the scaling variable "x-Bjorken" $= Q^2/2M\nu$. In his original papers (Bjorken, J.D., 1966 and 1970), he used the symbol ω which is defined as the inverse of x_{Bj}. In the Bjorken scaling limit (infinite momentum frame => asymptotic freedom of quarks), where ν and Q^2 go to infinity with x_{Bj} held fixed, both the spin dependent and the spin independent structure functions of ν and Q^2, scale to new "asymptotic" structure functions which depend only on x_{Bj}. The references vary on convention of definitions in terms of factors of M^2/ν (Bosted, P., 1993 and Ji, X., 1993). W_1 and W_2 scale to F_1 and F_2 where F_1 is the "Dirac" form factor which reduces to the nucleon electric charge in the limit as $q^2 => 0$ and F_2 is the "Pauli" form factor which reduces to the nucleon

anomalous magnetic moment. In a similar fashion, the spin-dependent structure functions G_1 and G_2 become the asymptotic spin-dependent structure functions g_1 and g_2.

The deep inelastic form factors may be studied using the techniques of current algebra's evaluated on the light cone defined by $x^\mu x_\mu = 0$. The theoretical mathematical techniques of evaluating current commutators in the infinite momentum approximation were pioneered by M. Gell-Mann of the California Institute of Technology and J. Schwinger of Harvard University. One valuable experimental prediction using these techniques was made by J.D. Bjorken at SLAC. He predicted the behavior of the difference of the first asymptotic structure functions of the neutron and proton. The Bjorken sum rule prediction, with third order QCD corrections (K. Abe *et al.*, 1994, B. Adeva *et al.*, SMC, 1993, D. Adams *et al.*, SMC, 1994, Bjorken, J.D., 1966 and 1970 and Feynman, R.P., 1972), is

$$\int_0^1 \left[g_1^P(x_{Bj}) - g_1^n(x_{Bj}) \right] dx_{Bj} \underset{\lim \nu, Q^2 \to \infty}{=} \left| \frac{g_A}{g_V} \right| \left(\frac{1}{6} - \frac{\alpha_s(Q^2)}{6\pi} - \frac{\alpha_s^2(Q^2)}{1.68\pi^2} \right). \tag{8}$$

The term in parenthesis on the right is a radiative correction where $\alpha_s(Q^2)$ is the energy-dependent strong coupling constant and g_A and g_V are the vector and axial-vector weak coupling constants from nucleon beta decay data. The ratio of g_A to g_V is found experimentally to be $1.257 +/- 0.003$.

Bjorken used strict U(6) local and global symmetry assumptions to derive his rule. This is the strictest treatment of quarks as it considers all 6 types known in the standard model. The vast majority of all physical processes, however, only involves the 3 types already mentioned, up, down and strange, and so dealing with only those three flavors of quarks should be an adequate approximation. This approximation was used by J. Ellis and R. Jaffe to make a prediction of the separate first asymptotic structure functions of the neutron and proton. The Ellis-Jaffe sum rule prediction, under the assumptions of global SU(3) flavor symmetry and no net polarization of the (strange) sea quarks, predicts (K. Abe *et al.*, 1994, B. Adeva *et al.*, SMC, 1993, D. Adams *et al.*, SMC, 1994, Ellis, J. and Jaffe, R., 1974) a value for g_1^P, integrated over values of Bjorken x from zero to one of $0.160 +/- 0.006$. The failure of the experimental evidence to support this prediction has caused great volumes of theoretical debate concerning the validity of the assumptions and possible explanations for the experimental results being lower than theory.

2. SLAC Experiment #143: "Nucleon Form Factors at 30 GeV"

The E143 "Nucleon Spin Structure" experiment used a polarized solid ammonia target as a source of polarized proton and deuteron scattering centers. The target was placed in the beamline at End Station 'A'. The electrons were accelerated to energies of 29.1 GeV. The electrons were polarized at the

source by a laser striking a strained GaAs epitaxial layer on the cathode and imparting the laser polarization to the liberated electrons (Abe, *et al.*, 1994 and McCarthy, J., *et al.*, 1993). The differential cross section for unpolarized lepton-hadron scattering, in the approximation of zero lepton mass ($M>>m$), is (Feynman, R.P., p. 128, 1972)

$$\frac{d^2\sigma_{unp}}{d\Omega dE'} = \left(\frac{\alpha}{Q}\right)^2 \left(\frac{E'}{E}\right)\left[2W_1 + \text{Cot}^2\left(\frac{\theta}{2}\right)W_2\right] = \sigma_{Mott}\left[W_2 + 2\text{Tan}^2\left(\frac{\theta}{2}\right)W_1\right]. \qquad (9)$$

For the large scattering angles of interest, this differential cross section is effectively equal to the unpolarized cross section, σ_{unp} (McCarthy, J., *et al.*, p. 3, 1993). The sign of the anti-symmetric hadron tensor in Equation (1) depends on the helicity of the proton in the center of mass reference frame. This means that the sum or difference of the cross sections for two scattering angles rotated by π radians will cancel either the symmetric or anti-symmetric part, respectively. The sum of the cross sections is, therefore, simply equal to twice σ_{unp}. The difference of the cross sections, however, is the experimental quantity of interest because it has a definite sensitivity to the initial nucleon polarization. It is (Ashman, J., *et al.*, p. 3, 1989, Hey, A.J.G. and Mandula, J.E., p.2610, 1972, Hughes, V.W. and Kuti, J., p. 216, 1983, McCarthy, J., *et al.*, p. 3, 1993)

$$\frac{d^2\sigma_{pol}}{d\Omega dE'} = \sigma^{\uparrow\uparrow} - \sigma^{\uparrow\downarrow} = \left(\frac{2\alpha}{Q^2}\right)^2 \left(\frac{E'}{E}\right)\left[M(E + E'\text{Cos}\theta)G_1 - Q^2 G_2\right]. \qquad (10)$$

The longitudinal asymmetry of scattering events, A_{long}, is then given in terms of these sums and differences of cross sections by (Abe, *et al.*, 1994, Bosted, 1994)

$$A_{long} = \frac{\sigma^{\uparrow\uparrow} - \sigma^{\uparrow\downarrow}}{\sigma^{\uparrow\uparrow} + \sigma^{\uparrow\downarrow}} = \frac{\sigma^{\uparrow\uparrow} - \sigma^{\uparrow\downarrow}}{2\sigma_{unp}} = \frac{2\left[\frac{M}{Q^2}(E + E'\text{Cos}\theta)G_1 - G_2\right]}{2W_1 + \text{Cot}^2\left(\frac{\theta}{2}\right)W_2}$$

$$= \left(\frac{N_- N_+}{N_- + N_+}\right)\left(\frac{C_N}{F_D P_B P_T}\right) + A_{RC} = \left(\frac{A_{exp} C_N}{F_D P_B P_T}\right) + A_{RC}, \qquad (11)$$

where P_B represents the beam polarization, P_T represents the target polarization, C_N is a correction for the effects of polarization of the unpaired proton in ^{15}N, N is the number of scattered electrons per incident charge for negative (N_-) and positive (N_+) beam helicity, A_{exp} is the observed experimental asymmetry, A_{RC} is the QED radiative correction for higher order terms of the fine structure constant and F_D is the ratio of

scattering events originating from polarizable protons to the total number of scattering events defined as (Ashman, J., *et al.*, p. 12, 1989 and Rondon, O.A., UVA-INPP-PUB-91-15, 1991) $N_P\sigma_P/\Sigma_yN_y\sigma_y$, where N_P is the number of polarizable protons per square centimeter, σ_p is the cross section for electron scattering from protons, and the summation in the denominator is over all possible scattering sources. A similar expression may be derived for the perpendicular asymmetry of scattering events, A_{perp}. The asymptotic, spin-dependent structure functions may then be derived from expressions in terms of the cross sections, kinematic variables and Bjorken x (Abe, K., *et al.*, E143, 1994, Bosted, 1993 and McCarthy, J., *et al.*).

The target used in End Station "A" (ESA) at SLAC for E143 contained grains of frozen ammonia that had been "radiation damaged" to produce "paramagnetic impurities" at various electron beam facilities including the Massachusetts Institute of Technology (MIT) Bates Laboratory, Stanford High Energy Physics Lab (HEPL), Naval Postgraduate School (NPS) and Saskatchewan Accelerator Laboratory (SAL). The ammonia in the target is bombarded with microwaves at a frequency to cause spin-flip transitions to polarized states around the impurities. The target material, target housing assembly and target polarization method are described in depth by the target group in various references (Abe, K., *et al.*, E143, 1994, Crabb, D.G., 1990 and McCarthy, J., *et al.*). The basic experimental setup of E143 in ESA is illustrated in Figure 2 below.
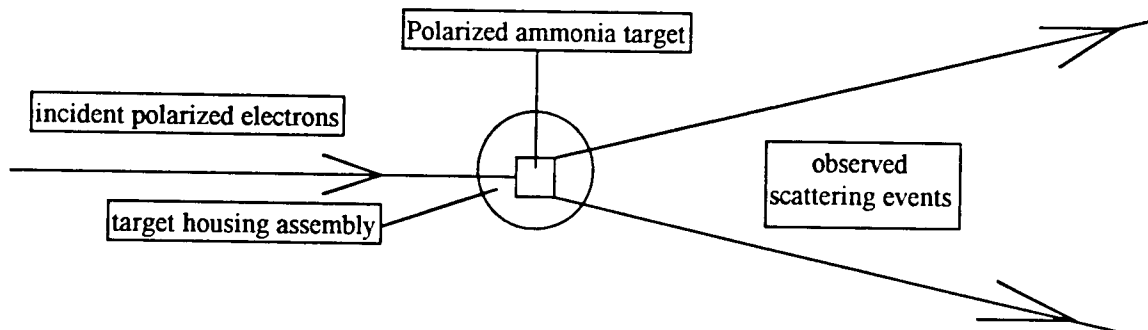

Figure 2. E143 experiment schematic. Polarized electrons are scattered by a polarized ammonia target.

III. TARGET MATERIAL THICKNESS MEASUREMENT

The ammonia target thickness measurements were made at SLAC from September 1993 through February 1994. The work was performed by the E143 Collaboration target group including myself and my advisor. The thickness was computed using the principle of attenuation of radiation through matter. A source of known intensity emits x-rays that pass through the unknown quantity of ammonia and the reduced intensity is detected on the other side. By comparison of the emitted and detected intensities, the amount of material passed through may be determined to a high degree of precision. The measurement apparatus was located in the small building adjacent to the controlled entrance to End Station A so that minimum changeout time and effort was required to transport the targets to and from the beamline and thickness measurement area. The torlon cells in the target insert sticks containing the ammonia material were perforated to allow the liquid helium bath to permeate and adequately cool the cell and yet not allow the beads of material that were jostled around in transit to be shaken out of the cell.

A. APPARATUS CONFIGURATION

A schematic representation of the liquid helium refrigerant dewar that contained the target insert and ammonia material as well as the locations of the quantities of interest is given in Figure 3 below.
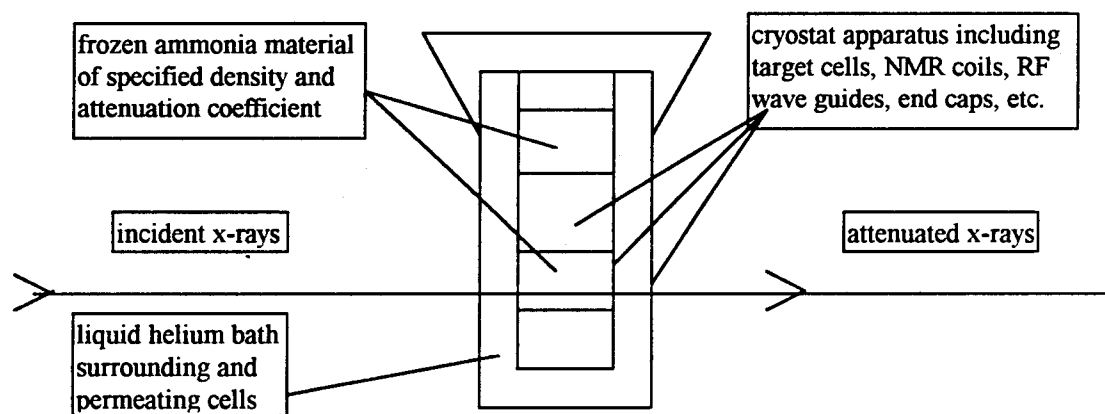

Figure 3. Schematic of target thickness determination method.

The following is a list of symbolic notation for the quantities used in the measurement:

t_y = effective linear thickness of material "y" in cm

t_{trgt} = target cell measured value: 3.00 +/- 0.03 cm

t_{amm} = effective linear thickness of ammonia in target cell

ρ_y = mass density of material "y" in $\dfrac{grams}{cm^3}$

$x_y = \rho_y t_y$ = mass thickness of material "y" in $\dfrac{grams}{cm^2}$

x_{He} = thickness of ^4He outside target cell

x'_{He} = thickness of ^4He inside target cell

x_{cryo} = thickness of cryostat, target assembly, etc.

x_{amm} = mass thickness of ammonia in target cell

μ_y = linear attenuation coefficient of "y" in cm^{-1}

$\left(\dfrac{\mu}{\rho}\right)_y$ = mass - attenuation coefficient of "y" in $\dfrac{cm^2}{gram}$

f_y = volume packing fraction of material "y"

f_{amm} = ammonia fraction of target volume = $\dfrac{t_{amm}}{t_{trgt}} = \dfrac{x_{amm}}{\rho_{amm} t_{trgt}}$

The mass-attenuation coefficients are calculated by the program "PHOTCOEF" (AIC software, 1993) running on a personal computer with a 386 processor. The entering arguments for the program are the chemical composition of the target material and the energy of the incident x-rays. For the 40 milli-Curie Americium 241 source used, the x-ray energy was 59.53 keV. This gives a computed value for the mass attenuation coefficient for ^4He of

$$\left(\frac{\mu}{\rho}\right)_{^4He} = 0.16534 \ \tfrac{cm^2}{gram}. \tag{12}$$

PHOTCOEF gives value for "normal" chemical compounds only and a correction is required for ammonia of different isotopic compositions. The photon interaction is an electromagnetic process governed by the charge distribution of a scattering center (molecule in this case). The actual values of the mass-attenuation coefficients, however, are derived in terms of interaction cross section per unit mass.

$$\left(\mu/\rho\right) \equiv \frac{n\sigma}{\rho} \equiv N_{Av}\left(\frac{\sigma}{A}\right) \equiv \frac{\text{cross section}}{\text{unit mass}}, \tag{13}$$

where A is the molecular weight, $n = N_{av}\rho/A$ is the number of scattering centers per unit volume and N_{Av} is Avogadro's number. Expanding upon this definition, we derive an expression for the mass-attenuation coefficients for $^{15}NH_3$ and $^{15}ND_3$ in terms of the mass-attenuation coefficient for $^{14}NH_3$.

$$\left[\frac{\mu_{^{15}NH_3}}{\rho_{^{15}NH_3}}\right] \equiv \left[\frac{\mu_{^{15}NH_3}}{\mu_{^{14}NH_3}}\right]\left[\frac{\rho_{^{14}NH_3}}{\rho_{^{15}NH_3}}\right]\left[\frac{\mu_{^{14}NH_3}}{\rho_{^{14}NH_3}}\right] = \left[\frac{(n\sigma)_{^{15}NH_3}}{(n\sigma)_{^{14}NH_3}}\right]\left[\frac{\rho_{^{14}NH_3}}{\rho_{^{15}NH_3}}\right]\left[\frac{\mu_{^{14}NH_3}}{\rho_{^{14}NH_3}}\right]. \tag{14}$$

Note that using this derivation and the definitions at the beginning of this Section, it is observed that the expression for the Dilution Factor used in the expression for A_{long} can also be written as:

$$F_D = \frac{N_{Av}\sigma_P\left(x/A\right)_P}{\sum_y N_{Av}\sigma_y\left(x/A\right)_y} = \frac{\left[\left(\mu/\rho\right)\times x\right]_P}{\sum_y\left[\left(\mu/\rho\right)\times x\right]_y}. \tag{15}$$

We assume that the x-ray scattering amplitudes is proportional to the charge distribution of the scattering center, independent of its mass, i.e. $\sigma_{15NH3} = \sigma_{14NH3}$. With this assumption, the expression for (μ/ρ) for $^{15}NH_3$ in terms of (μ/ρ) for $^{14}NH_3$ from Equation (14) can be simplified.

$$\left[\frac{\mu_{^{15}NH3}}{\rho_{^{15}NH3}}\right] = \left[\frac{\rho_{^{15}NH3}}{\rho_{^{14}NH3}}\right]\left[\frac{A_{^{14}NH3}}{A_{^{15}NH3}}\right]\left[\frac{\rho_{^{14}NH3}}{\rho_{^{15}NH3}}\right]\left[\frac{\mu_{^{14}NH3}}{\rho_{^{14}NH3}}\right] = \left[\frac{A_{^{14}NH3}}{A_{^{15}NH3}}\right]\left[\frac{\mu_{^{14}NH3}}{\rho_{^{14}NH3}}\right]. \tag{16}$$

Note that it is the ratio of the molecular weights that determines the isotopic mass-attenuation coefficient. At 59.53 keV, the coefficients for "normal" $^{14}NH_3$ and the isotopes used in the experiment are

$$\begin{aligned}
\left(\mu/\rho\right)_{^{14}NH_3} &= 0.20798 \ \tfrac{cm^2}{gram} \\
\left(\mu/\rho\right)_{^{15}NH_3} &= 0.19643 \ \tfrac{cm^2}{gram} = \left(^{17}/_{18}\right)\left(\mu/\rho\right)_{^{14}NH_3} \\
\left(\mu/\rho\right)_{^{15}ND_3} &= 0.16836 \ \tfrac{cm^2}{gram} = \left(^{17}/_{21}\right)\left(\mu/\rho\right)_{^{14}NH_3}
\end{aligned}, \tag{17}$$

where the isotopes are corrected by the ratio of the number of nucleons. Binding energy corrections are negligible, amounting to less than 0.05% (Walker, F.W., 1984). The mass density values used are

$$
\begin{array}{rcl}
\rho_{He} & = & 0.128 \pm 0.003 \ \frac{grams}{cm^3} \\
\rho_{He} & = & 0.917 \pm 0.001 \ \frac{grams}{cm^3} \\
\rho_{He} & = & 1.056 \pm 0.001 \ \frac{grams}{cm^3}
\end{array} \right] \tag{18}
$$

All densities are for 4.0 +/- 0.1 Kelvin and liquid helium vapor pressure (Anderson, H.J., 1989). The uncertainty in the temperature is a conservative estimate and the densities apply within the range.

There are two experimental configurations which must be considered. In the first setup, the cryostat assembly is full of helium at 4 K with a target stick inserted. The x-ray beam is scanned across the face of a cell that contains the unknown thickness of solid ammonia. The second setup is identical except that the ammonia crystals have been removed and the target cell is empty. The exposure time for both configurations is the same, so Poisson statistics apply (Taylor, J.R., 1982). The resultant x-ray intensities, "I_{am}" and "I_{empty}," after traversing the targets are:

$$
I_{amm} = I_0 e^{-\left\{ \left(\frac{\mu}{\rho} \right)_{cryo} x_{cryo} + \left(\frac{\mu}{\rho} \right)_{He} \left(x_{He} + x'_{He} \right) + \left(\frac{\mu}{\rho} \right)_{amm} x_{amm} \right\}} \tag{19}
$$

for the x-rays passing through an ammonia filled cell and

$$
I_{empty} = I_0 e^{-\left\{ \left(\frac{\mu}{\rho} \right)_{cryo} x_{cryo} + \left(\frac{\mu}{\rho} \right)_{He} \left(x_{He} + x'_{He} + x_{amm} \right) \right\}} \tag{20}
$$

for the x-rays passing through an empty cell. The terms with the subscript "cryo-" refer to the effects of the experimental apparatus and include all support structure, NMR coils, target cells, etc. These are too complex to be easily evaluated but they are identical for both situations. Consequently, taking the ratio cancels their effects.

$$
\left(\frac{I_{empty}}{I_{amm}} \right) = e^{-f_{amm} t_{trgt} \rho_{amm} \left(\left(\frac{\rho_{He}}{\rho_{amm}} \right) \left(\frac{\mu}{\rho} \right)_{He} - \left(\frac{\mu}{\rho} \right)_{amm} \right)} \tag{21}
$$

Taking the logarithm of each side and rearranging terms gives the desired expression for the **volume packing fraction** in a target cell.

$$f_{amm} = \frac{\ell n\left(I_{empty}/I_{amm}\right)}{t_{trgt}\rho_{amm}\left(\left(\mu/\rho\right)_{amm} - \left(\rho_{He}/\rho_{amm}\right)\left(\mu/\rho\right)_{He}\right)} \quad . \tag{22}$$

The denominator in this expression can be computed independently of the x-ray measurement and has values of 0.47689 for the NH_3 and 0.46988 for the ND_3. The **mass-thickness** of ammonia in a target cell is consequently:

$$x_{amm} = t_{trgt}\rho_{amm}f_{amm} = \frac{\ell n\left(I_{empty}/I_{amm}\right)}{\left(\left(\mu/\rho\right)_{amm} - \left(\rho_{He}/\rho_{amm}\right)\left(\mu/\rho\right)_{He}\right)} \quad . \tag{23}$$

The denominator has a value of 0.17335 for the NH_3 and 0.14832 for the ND_3. Note that the effective mass-attenuation coefficient of helium in the denominator is suppressed relative to the mass-attenuation coefficient of ammonia by a factor of the ratio of their densities (< 0.143). Thus while each mass-attenuation coefficients is comparable in magnitude, the ammonia term contributes $(1/0.143) = 7$ times more in the denominator. This observation will have implications in the next section.

B. EXPERIMENTAL PROCEDURES

We assume that if $x,...,z$ are measurements used to compute the function $q(x,...,z)$, and if the uncertainties in $x,...,z$ are independent and random, then the uncertainty in the computed function q is given by (Taylor, 1982):

$$\delta q = \sqrt{\left(\frac{\partial q}{\partial x}\delta x\right)^2 + ... + \left(\frac{\partial q}{\partial z}\delta z\right)^2} \quad . \tag{24}$$

We treat the intensity measurements as satisfying Equation (24). The uncertainty in the packing fraction, Equation (22), and the mass-thickness, Equation (23), result from uncertainties in the attenuation coefficients, material densities and the x-ray intensity measurements which are independent variables. The largest source of uncertainty is the calculated mass-attenuation coefficient for ammonia. This uncertainty, however, is not random, but is a contribution to the systematic error. The contribution from the ammonia mass-attenuation coefficient is seven times more significant than that from helium. The accurate knowledge of the x-ray energy is also less significant. We maintain four digits of accuracy rather than round the source energy up to 60 keV but the effect of lack of precision in the x-ray energy is minimal. For example, using 60.00 keV, which is 0.8% higher than the actual x-ray energy, the denominator in Equation (23) becomes 0.17400 resulting in a 0.4% decrease in thickness. Ignoring the systematic errors, the fractional uncertainty in the mass-thickness is a function of intensities only.

$$\frac{\delta x_{amm}}{x_{amm}} = \frac{\sqrt{\left(\frac{\delta I_{empty}}{I_{empty}}\right)^2 + \left(\frac{\delta I_{amm}}{I_{amm}}\right)^2}}{\ell n\left(\frac{I_{empty}}{I_{amm}}\right)} = \frac{\sqrt{\frac{(I_{empty}+I_{amm})}{(I_{empty}I_{amm})}}}{\ell n\left(\frac{I_{empty}}{I_{amm}}\right)} = \frac{\sqrt{\frac{\left[1+\left(I_{empty}/I_{amm}\right)\right]}{\left(I_{empty}/I_{amm}\right)\left(I_{amm}\right)}}}{\ell n\left(\frac{I_{empty}}{I_{amm}}\right)}, \tag{25}$$

where the uncertainty in intensities has been evaluated as the square root of the number of counts. The last step is to show explicitly that as thickness increases, the error decreases as the ratio I_{empty}/I_{amm} goes to infinity. This is justified because identical counting times were used. The quantities of interest, mass-thickness and volume packing fraction, describe all of the material in a given basket. This means that the intensities used for our calculations are the sums of the 21 intensities from each scan position. This greatly improves the overall accuracy as point to point fluctuations are averaged throughout the entire volume of a cell. Note that the difference between the average of the logarithms of the intensity ratios and the logarithm of the average of the intensity ratios is within 0.6%. The statistical error on the final values ranges from 0.85% to 1.3%. The systematic uncertainty in the computer tabulated values of the attenuation cross sections are not well established experimentally, but theoretically, for small Z, they are expected to be in the 2-5% range (McMaster, V., et al., 1967).

The ammonia samples to be measured were placed in a second liquid helium cooled cryostat after being transferred from the actual target assembly in ESA. The position of a target cell in relation to the lab table outside the cryostat was determined to better than 0.5 mm. The target was exposed to the [241]Am source for five minutes per scan point. The configuration for the thickness measurement is shown in Figure 4 below.
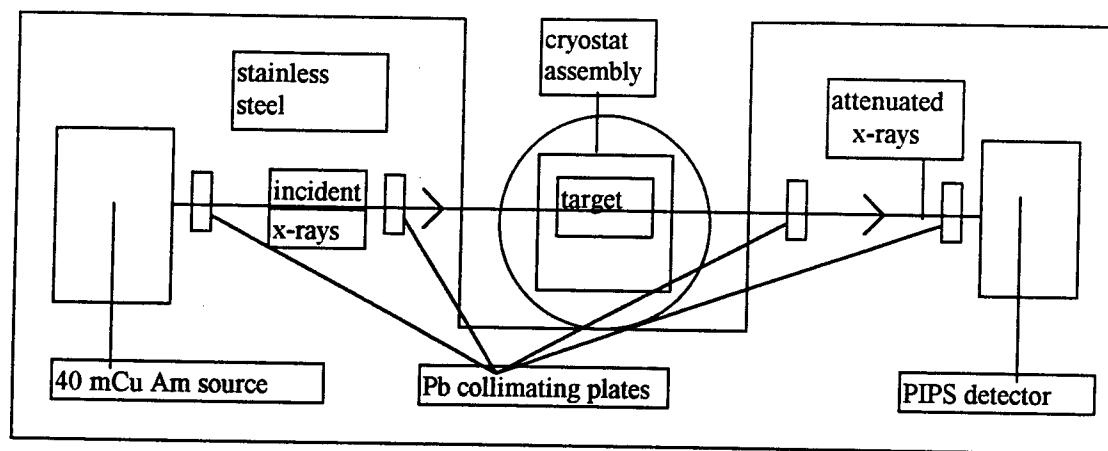
Figure 4. Schematic of target thicknessdetermination apparatus.

One important difference of the target configuration used in the thickness measurement and in the electron beam runs is that the helium bath in the thickness measurement was at 4 K which is above the lambda point of helium (2.18 K), while that in the ESA runs was below the lambda point. In the ESA electron beam runs the helium density is approximately 13% greater than during the thickness measurement. Incorrectly applying the greater helium density of 0.145 grams per cubic cm would increase the denominator in Equation (22) to 0.46847 for NH_3 and 0.46144 for ND_3, resulting in a 1.8% increase in computed packing fraction. The packing fraction is a measurement of the physical dimensions of the ammonia, irrespective of the surrounding helium. The packing fraction which we have measured is the value which should be used.

The source was set on one end of a rectangular steel support plate. A large notch was cut out of the side of the support plate in the center so that the tailpiece of the helium dewar could be set in. The support plate was mounted on a milling machine drive that allowed a Cartesian coordinate mapping of the target face by adjusting the support plate after each five minute scan point measurement. At several points along the beam path there are lead collimating plates with holes of five mm diameter. It is these holes that define the spots that overlap and cover the entire target face. The outermost one mm ring was not scanned by the electron beam in ESA and so was omitted from the thickness mapping. The face area of a target window is covered, with minimal overlap, by 21 scan points as shown in Figure 5 below.

Figure 5. Pattern of 21 scan points of 5 mm diameter each. Target face is 25.4 mm diameter.

Because of the presence of Cu/Ni wire coils for NMR measurements of the target polarization, the assignment of scan point centers might have an inordinate influence on the target thickness measurement. To insure that this was not the case, new scan point locations were assigned to points 7, 9, 15 and 17. These new points are the "primed" points 7', 9', 15', 17'. The primed scan points have the same horizontal coordinates as the unprimed points but are 0.03 inches closer to the center in the vertical direction. Stick number one has no prime point measurements as it was done before this coverage effect was realized. As seen in Tables 6 through 12, the use of the original or the primed points results in very little difference in the final thickness results.

The detector was a Canberra Passivated Implanted Planar Silicon (PIPS) with associated FET input preamplifier (Canberra products catalog, 1989). Calibration tests were performed before measurements began to ensure that the detector efficiency and resolution were constant in time over a period of several hours. The output signal was displayed with "Nucleus-II" personal computer analyzer software (Oxford/Tennelec Industries, 1990). The distance from the [241]Am source to the detector was 28.5 cm.

18

IV. DATA AND ANALYSIS

Our results were tabulated using "Excel" spreadsheet software (Microsoft Corp., 1993). There are seven data sets, each consisting of a top cell and a bottom cell entry. All the ammonia material for stick numbers 1 and 3 was radiated at the Stanford High Energy Physics Lab 60 MeV linac, but the ND_3 for stick number 2 was from Bates Lab while the NH_3 was radiated at the Naval Postgraduate School in Monterey. The data was divided by date. The data for stick number 1 is from mid January, 1994 and did not use the "prime" raster positions. The data set for stick number 2a is from early January 1994 and did not use the "prime" raster positions, the data set for stick number 2b was taken later that month and also did not use the primed scan points. The data for stick number 2b prime is identical to number 2b except for using the values at the primed scan point locations. The data set for stick number 3a is from early January, 1994, while the data set for stick number 3b was taken in mid February, 1994 after final exposure in ESA. The data for stick number 3b prime is identical to number 3b except for using the values at the primed scan point locations. The data analysis software (Oxford/Tennelec, 1990) gives count intensities in both un-integrated total intensities and integrated intensities with uniform "background" energies subtracted out. Our calculations use the first value. Our assumption in including the "background" from the spectrum was that it was directional from the source due to our precautionary shielding of the detector and collimating of the beam. Comparison to runs of much longer times with no source show that true atmospheric background was completely negligible to the source intensity and that anything getting to the detector through one type of cell was getting through to the other also. The intensity calculations of Equations (19) through (23) assume total counts from all possible sources.

A. ASSIGNMENT OF VALUES TO SCAN POINTS

The columns of the data are arranged in tables as follows; "Scan Point" is the numbered position of the five mm diameter circle of the pattern of 21 used to cover the face of a target. The next two columns are grid coordinates of the relative positions of the scan points. The fourth column is the integrated intensity, including "background," of the "empty" target. The fifth column is the same data for a corresponding "full" target, again including the background since we are subtracting logarithms and so must include the entire sum of intensities at the detector. The sixth column takes the logarithm of the ratio of the fourth to the fifth column. The "Mass-Thik" column performs Equation (23) by dividing the sixth column by the given denominator to give a value for the mass thickness in grams per square centimeter. Column number eight gives a normalized value for the mass thickness by dividing each point by the average of the middle nine scan points (2 through 4, 7 through 9 and 15 through 17). Column number nine gives the

packing fraction corresponding to the thickness value in the seventh column by performing Equation (22). The last column gives the fractional uncertainty in intensity used in Equation (25).

The bottom two entries of column numbers four and five average the intensities above them over all 21 points, or only the center 9, while for the last five column calculations, the algebraic operation is performed on the averages derived in the bottom two entries of column number six. The difference between the average of the logarithms and the logarithm of the averages is negligible. This was determined by having the final values of column numbers six through ten calculated by averaging over the 21 points in the column above them rather than operating on the values up the row to their left. The numbers obtained either way differ by less than 0.2%.

The final results for the target thickness and packing fraction measurement are displayed, with their random errors, in Table 1 below.

Stick Number	Dates in ESA Beamline	Sample Material	Ammonia Cell Type	Thickness grams/cc	Random Error	Packing Fraction	Random Error
1;	1/13/94–	Stanford	Top-NH3	1.729	0.009	0.629	0.003
	1/23/94	Stanford	Bot-NH3	1.64	0.009	0.596	0.003
2a;	12/1/93–	Bates	Top-ND3	1.462	0.008	0.532	0.003
	1/7/94	NPS	Bot-NH3	1.747	0.009	0.551	0.003
2b;	12/1/93–	Bates	Top-ND3	1.53	0.008	0.556	0.003
	1/7/94	NPS	Bot-NH3	1.85	0.01	0.583	0.003
2b';	12/1/93–	Bates	Top-ND3	1.5	0.008	0.546	0.003
	1/7/94	NPS	Bot-NH3	184	0.01	0.58	0.003
3a;	1/7/94–	HEPL	Top-ND3	1.384	0.008	0.503	0.003
	1/13/94	HEPL	Bot-NH3	1.643	0.009	0.519	0.003
3b;	1/23/94–	HEPL	Top-ND3	1.409	0.008	0.512	0.003
	completion	HEPL	Bot-NH3	1.701	0.009	0.537	0.003
3b';	1/23/94–	HEPL	Top-ND3	1.41	0.008	0.512	0.003
	completion	HEPL	Bot-NH3	1.7	0.009	0.537	0.003

Table 1. Target thickness measurement results.

B. THICKNESS AS A FUNCTION OF HEIGHT

An important question about the experimental results is whether there was a settling effect and the average thickness decreases with height. Table 2 shows the data sets arranged by vertical elevation on the target face, averaged over horizontal scan points. It is seen that the effect of the primed scan points is minor and that the greatest difference due to using them over the unprimed points is of the order of 0.5% for stick number 3b and Stick number 2b ND_3, and 2.0% for the NH_3 in stick number 2b. In all four cases, the correction for primed scan points produced lower thickness values. Tables 3 through 12 and Figures 6 through 15 show the variation of target thickness as a function of vertical position. Note that in Figures 6 through 15, the error bars shown are the range of the horizontal values at a given vertical height. This error is larger for the central positions because there are more data points there and so the range of values spanned by the average is greater. All of the graphs appear to be consistent with thickness decreasing as height increases except stick number 3b prime which appears relatively flat in comparison.

In order to visualize the non-uniformity of the target, Figure 16 shows the grid pattern of (unprimed) data points for stick number 1, bottom cell. Figure 17 presents a three dimensional view of the target thickness for the bottom cell of that stick, and Figure 18 is a contour plot of the same data. The primed scan points are shown in Figure 19. Figures 20 and 21 are the three dimensional and contour view of the bottom cell of stick number 3b prime and show a more uniform thickness which explains the relative flatness observed in Figure 14.

The measurement of the target thickness was simultaneously performed by two other groups: the team of Dr. Ingo Sick and Beni Zihlmann from Basel Switzerland and the team of Dr. Peter Bosted from the American University, Washington, D.C. and Todd Averett from the University of Virginia at Charlottesville. The Basel group also used a radiation attenuation measurement, but used a solid carbon and liquid ammonia target produced and measured in Basel, Switzerland as reference targets for their ratios. The second group compared event rates for each sample after the fact from the actual experimental data to a carbon reference target. As of November, 1994, there was still some error between the three sets of data. The Averett/Bosted data is approximately in the middle of NPS values, which are all lower, and the Basel values, which are all higher. The sources of disagreement and systematic error have not been agreed upon as yet by the three groups, but by allowing a large enough uncertainty to encompass the range of the three data sets for ammonia thickness, the final uncertainty in the Dilution Factor is of the order of (Bosted, 1994) 2%. This is within the desired accuracy of the initial proposal (McCarthy, J., *et al.*, 1993).

APPENDIX. GRAPHIC REPRESENTATIONS OF DATA SETS

	y-axis	AvgThik	PacFrac.		y-axis	AvgThik	PacFrac.
Stick #1	0.31	1.508	0.548164	Stick #1	0.31	1.474	0.535805
Top-NH3	0.26	1.072	0.389676	Bot-NH3	0.26	1.727	0.627772
Radiated	0.17	1.274	0.463104	Radiated	0.17	1.347	0.48964
at	0	1.762	0.640494	at	0	1.548	0.562704
HEPL,	-0.17	2.13	0.774264	HEPL,	-0.17	1.856	0.674664
Stanford	-0.3	2.26	0.821519	Stanford	-0.3	1.834	0.666667
	-0.35	2.505	0.910578		-0.35	1.961	0.712832
Stick #2a	0.31	1.046	0.330177	Stick #2a	0.31	1.218	0.442748
Top-ND3	0.26	1.889	0.596275	Bot-NH3	0.26	0.6743	0.245111
Radiated	0.17	1.2	0.378788	Radiated	0.17	1.363	0.495456
at	0	1.841	0.581124	at	0	1.533	0.557252
Bates,	-0.17	2.448	0.772727	NPS,	-0.17	1.318	0.479099
MIT	-0.3	1.955	0.617109	Monterey	-0.3	1.534	0.557615
	-0.35	2.152	0.679293		-0.35	2.648	0.962559
Stick #2b	0.31	1.304	0.411616	Stick #2b	0.31	0.7451	0.270847
Top-ND3	0.26	1.554	0.49053	Bot-NH3	0.26	1.15	0.41803
Radiated	0.17	1.659	0.523674	Radiated	0.17	1.068	0.388222
at	0	1.638	0.517045	at	0	1.761	0.640131
Bates,	-0.17	2.283	0.720644	NPS,	-0.17	1.818	0.660851
MIT	-0.3	2.018	0.636995	Monterey	-0.3	1.658	0.60269
	-0.35	2.463	0.777462		-0.35	2.662	0.967648
Stick #2b	0.31	1.304	0.411616	Stick #2b	0.31	0.7451	0.270847
Top-ND3	0.26	1.554	0.49053	Bot-NH3	0.26	1.15	0.41803
Radiated	0.14	1.631	0.514836	Radiated	0.14	1.061	0.385678
at	0	1.638	0.517045	at	0	1.761	0.640131
Bates,	-0.14	2.264	0.714646	NPS,	-0.14	1.704	0.619411
MIT	-0.3	2.018	0.636995	Monterey	-0.3	1.658	0.60269
	-0.35	2.463	0.777462		-0.35	2.662	0.967648
Stick #3a	0.31	2.043	0.644886	Stick #3a	0.31	1.45	0.527081
Top-ND3	0.26	1.891	0.596907	Bot-NH3	0.26	0.8156	0.296474
Radiated	0.17	1.161	0.366477	Radiated	0.17	1.901	0.691021
at	0	2.37	0.748106	at	0	1.276	0.463831
HEPL,	-0.17	1.184	0.373737	HEPL,	-0.17	1.055	0.383497
Stanford	-0.3	2.182	0.688763	Stanford	-0.3	1.821	0.661941
	-0.35	0.7641	0.241193		-0.35	1.153	0.41912
Stick #3a	0.31	0.9718	0.306755	Stick #3b	0.31	0.9053	0.32908
Top-ND3	0.26	0.87	0.274621	Bot-NH3	0.26	1.138	0.413668
Radiated	0.17	1.52	0.479798	Radiated	0.17	1.393	0.506361
at	0	1.854	0.585227	at	0	1.462	0.531443
HEPL,	-0.17	1.877	0.592487	HEPL,	-0.17	1.484	0.53944
Stanford	-0.3	2.513	0.793245	Stanford	-0.3	1.521	0.55289
	-0.35	1.953	0.616477		-0.35	1.696	0.616503
Stick #3b	0.31	0.9718	0.306755	Stick #3b	0.31	0.9053	0.32908
Top-ND3	0.26	0.87	0.274621	Bot-NH3	0.26	1.138	0.413668
Radiated	0.14	1.51	0.476641	Radiated	0.14	1.372	0.498728
at	0	1.854	0.585227	at	0	1.462	0.531443
HEPL,	-0.14	1.885	0.595013	HEPL,	-0.14	1.509	0.548528
Stanford	-0.3	2.513	0.793245	Stanford	-0.3	1.521	0.55289
	-0.35	1.953	0.616477		-0.35	1.696	0.616503

Table 2. Variation of data sets with vertical position.

```
Stick1  -0.35  2.552595  2.457405   2.505
  Top   -0.3   2.463802  2.024597   2.26
15NH3   -0.17  2.471171  1.51307    2.13
sample   0     2.562405  1.20705    1.762
 from    0.17  2.29905   0.188916   1.274
HEPL     0.26  1.159399  0.984245   1.072
         0.31  1.536652  1.479348   1.508
```

Table 3. Stick #1 top cell variation of thickness for a given vertical position.

Figure 6. Stick #1 top cell variation of thickness for a given vertical position.

```
Stick1  -0.35  2.007672  1.914328   1.961
Bottom  -0.3   2.017496  1.85839    1.834
15NH3   -0.17  1.967024  1.683543   1.856
sample   0     1.970723  1.455216   1.548
 from    0.17  2.017496  0.924131   1.347
HEPL     0.26  1.837073  0.909016   1.727
         0.31  1.508934  1.439066   1.474
```

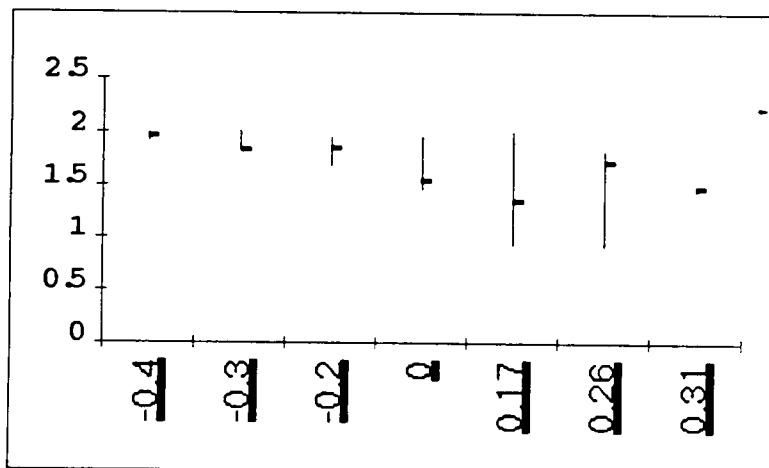Table 4. Stick #1 bottom cell variation of thickness for a given vertical position.

Figure 7. Stick #1 bottom cell variation of thickness for a given vertical position.

```
Stick2a   -0.35   2.202357   2.101643   2.152
   Top     -0.3   2.079346   1.833116   1.955
 15ND3    -0.17    2.82132   2.123782   2.448
sample        0   2.815392   0.872776   1.841
  from     0.17   1.790826   0.746651    1.2
Bates,     0.26   2.135189   1.648595   1.889
   MIT     0.31   1.078426   1.013574   1.046
```

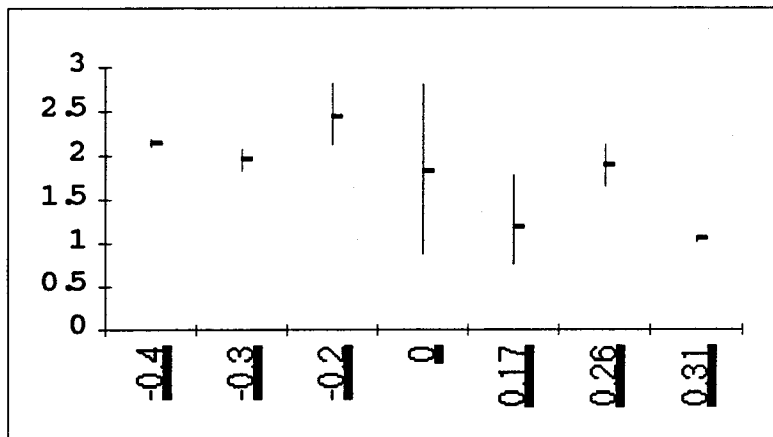Table 5. Stick #2a top cell variation of thickness for a given vertical position.

Figure 8. Stick #2a top cell variation of thickness for a given vertical position.

```
Stick2a  -0.35   2.698577   2.597423   2.648
 Bottom   -0.3   1.688775   1.381274   1.534
  15NH3  -0.17   1.673259   1.022169   1.318
 sample      0    2.57016   0.574774   1.533
   from   0.17   1.905008   0.696056   1.363
    NPS   0.26   1.480258   1.409742   1.445
          0.31   1.251008   1.184992   1.218
```

Table 6. Stick #2a bottom cell variation of thickness for a given vertical position.
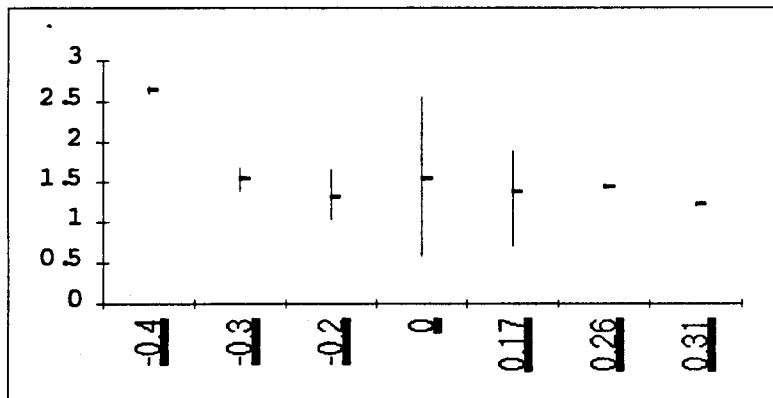

Figure 9. Stick #2a bottom cell variation of thickness for a given vertical position.

```
Stick2b  -0.35  2.517679  2.408321  2.463
   Top   -0.3   2.074229  1.961414  2.017
 15ND3   -0.14  2.584666  1.975662  2.283
primed    0     1.870592  1.345529  1.638
sample   0.14   1.884318  1.48413   1.659
  from   0.26   1.655698  1.454331  1.544
 Bates   0.31   1.340512  1.267488  1.304
```

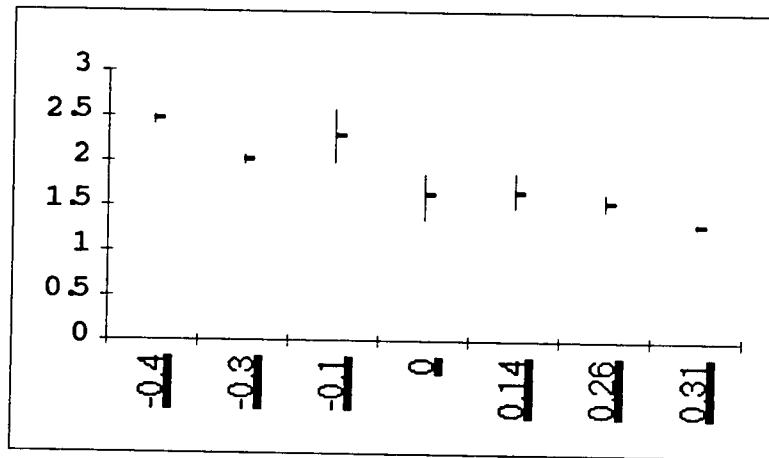Table 7. Stick #2b top cell variation of thickness for a given vertical position.

Figure 10. Stick #2b top cell variation of thickness for a given vertical position.

```
Stick2b  -0.35  2.712844  2.611156  2.662
Bottom   -0.3   1.75257   1.563566  1.658
 15NH3   -0.14  2.383421  1.467145  1.818
primed    0     2.115941  1.387238  1.761
sample   0.14   1.774385  0.400363  1.068
  from   0.26   2.191443  0.141819  1.15
   NPS   0.31   0.770359  0.719841  0.745
```

Table 8. Stick #2b bottom cell variation of thickness for a given vertical position.
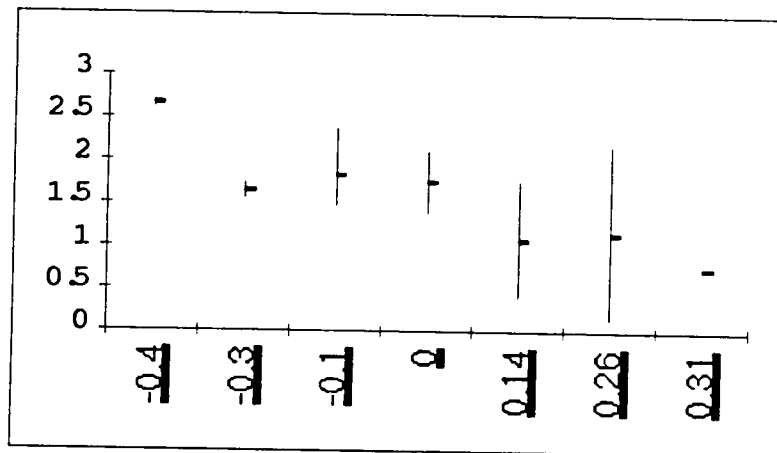

Figure 11. Stick #2b bottom cell variation of thickness for a given vertical position.

```
Stick3a   -0.35   0.792983 0.735217   0.764
   Top    -0.3    3.119259 1.264312   2.182
 15ND3    -0.17   1.723344  0.6168    1.184
second     0      3.108664 1.738526   2.37
sample    0.17    1.620907 0.724594   1.161
  from    0.26    2.066675 1.716799   1.891
  HEPL    0.31    2.088559 1.961414   2.043
```

Table 9. Stick #3a top cell variation of thickness for a given vertical position.
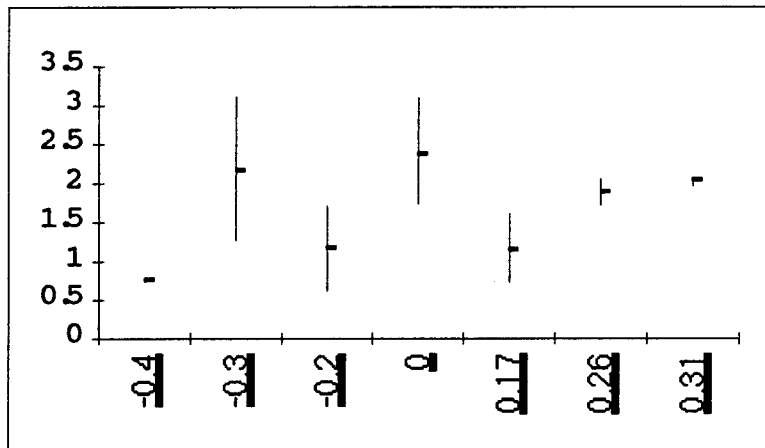

Figure 12. Stick #3a top cell variation of thickness for a given vertical position.

```
Stick3a   -0.35    1.18563   1.12037   1.153
Bottom     -0.3    2.259965 1.391753  1.821
 15NH3    -0.17    1.531927 0.589776  1.055
second      0      1.713525 1.054825  1.276
sample    0.17     2.215353 1.053644  1.901
  from    0.26     1.03618  0.601625  0.816
  HEPL    0.31     1.486105 1.413895   1.45
```

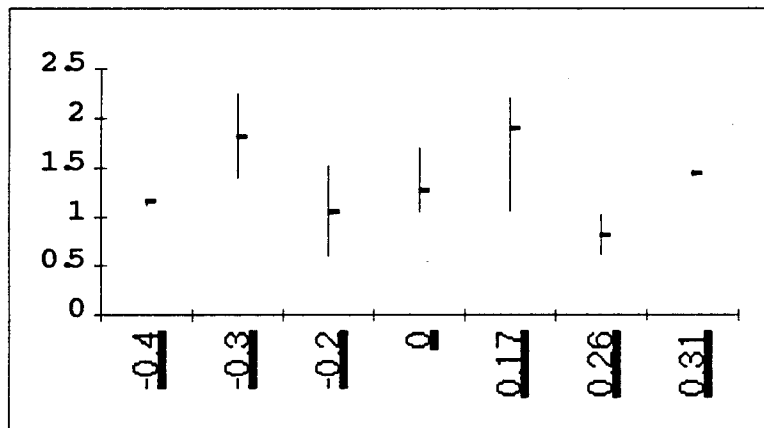Table 10. Stick #3a bottom cell variation of thickness for a given vertical position.

Figure 13. Stick #3a bottom cell variation of thickness for a given vertical position.

Stick3b	-0.35	2.001434	1.904566	1.953
Top	-0.3	2.722599	2.304404	2.513
15ND3	-0.14	2.043904	1.728763	1.885
primed	0	1.96026	1.713856	1.854
second	0.14	1.737875	1.320112	1.51
HEPL	0.26	1.010576	0.732108	0.87
sample	0.31	1.001926	0.941674	0.972

Table 11. Stick #3b top cell variation of thickness for a given vertical position.
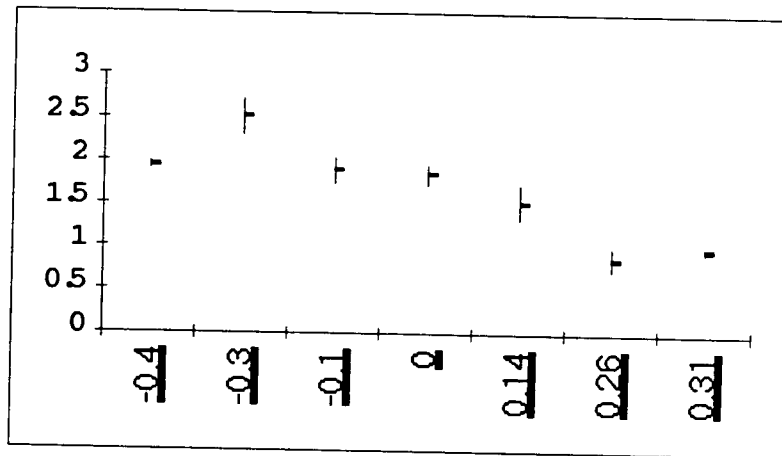

Figure 14. Stick #3b top cell variation of thickness for a given vertical position.

Stick3b	-0.35	1.736704	1.655296	1.696
Bottom	-0.3	1.678579	1.366115	1.521
15NH3	-0.14	1.68501	1.396057	1.509
primed	0	1.679196	1.210389	1.462
second	0.14	1.538471	1.220547	1.372
HEPL	0.26	1.240313	1.038756	1.138
sample	0.31	0.932784	0.877217	0.905

Table 12. Stick #3b bottom cell variation of thickness for a given vertical position.
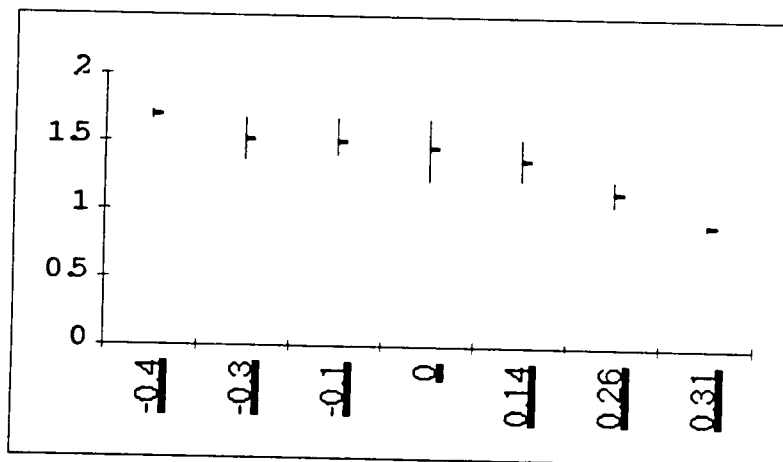

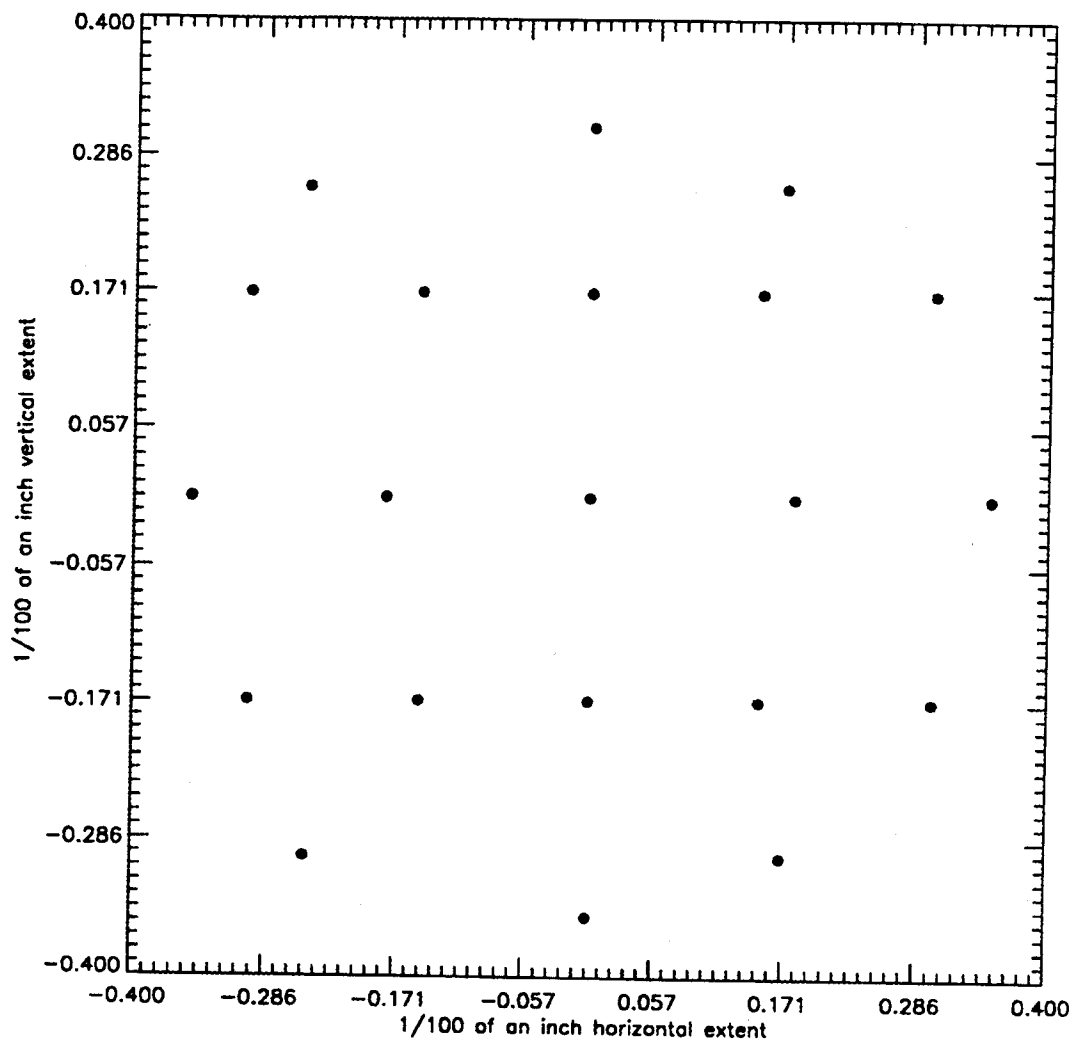Figure 15. Stick #3b bottom cell variation of thickness for a given vertical position.

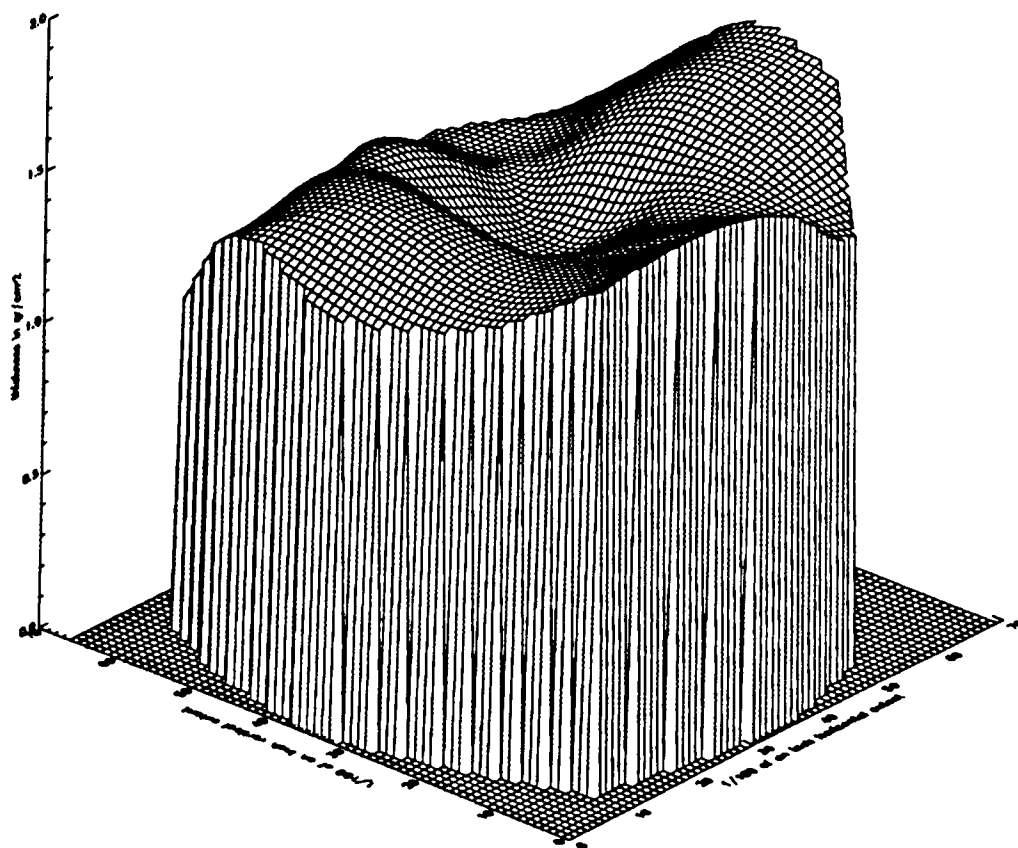Figure 16. Centers of the "unprimed" scan points #'s 1-21.

Figure 17. Thickness variation for stick #1, bottom, Bates NH₃ target. Data presented in Table 1.
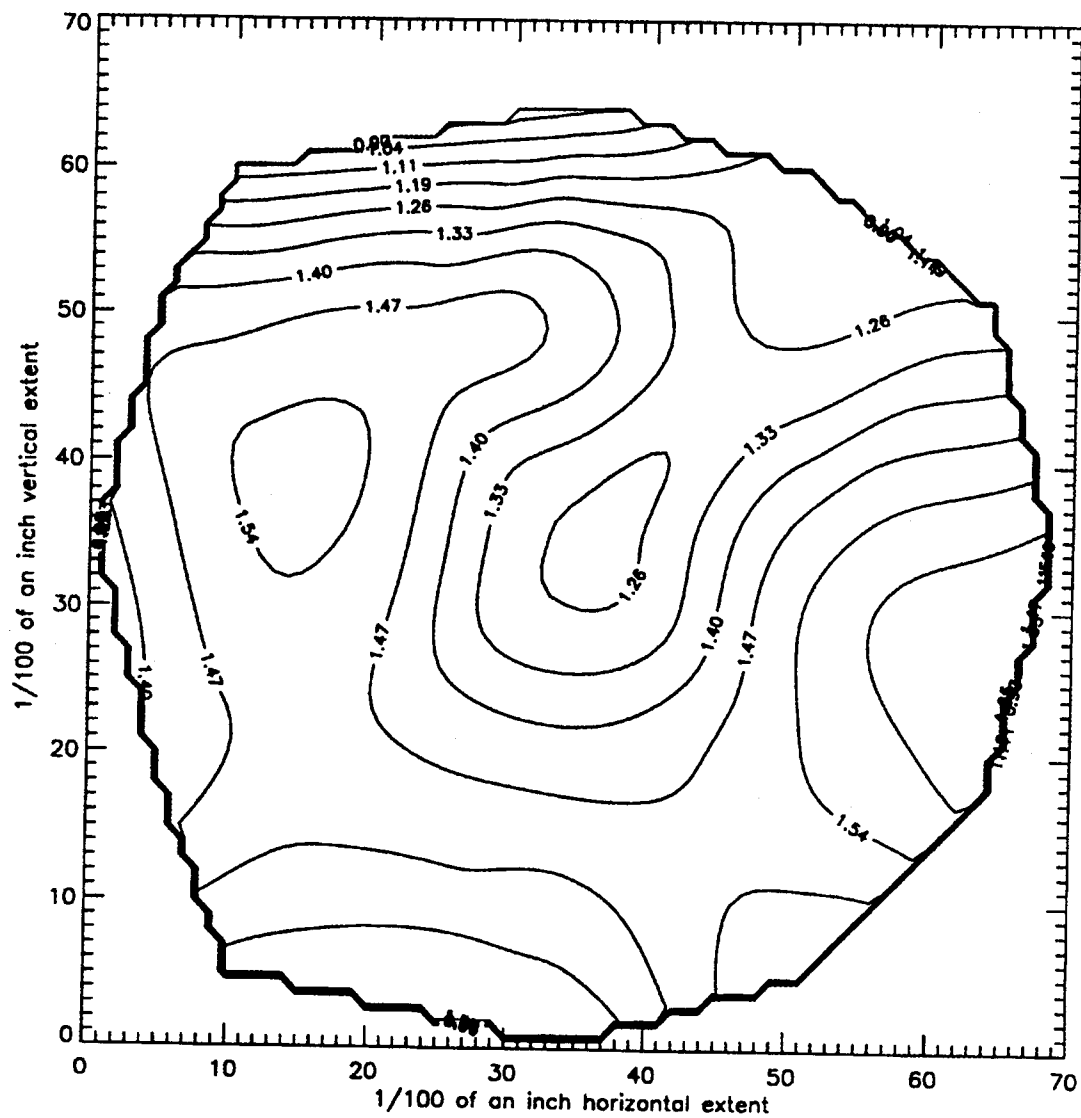
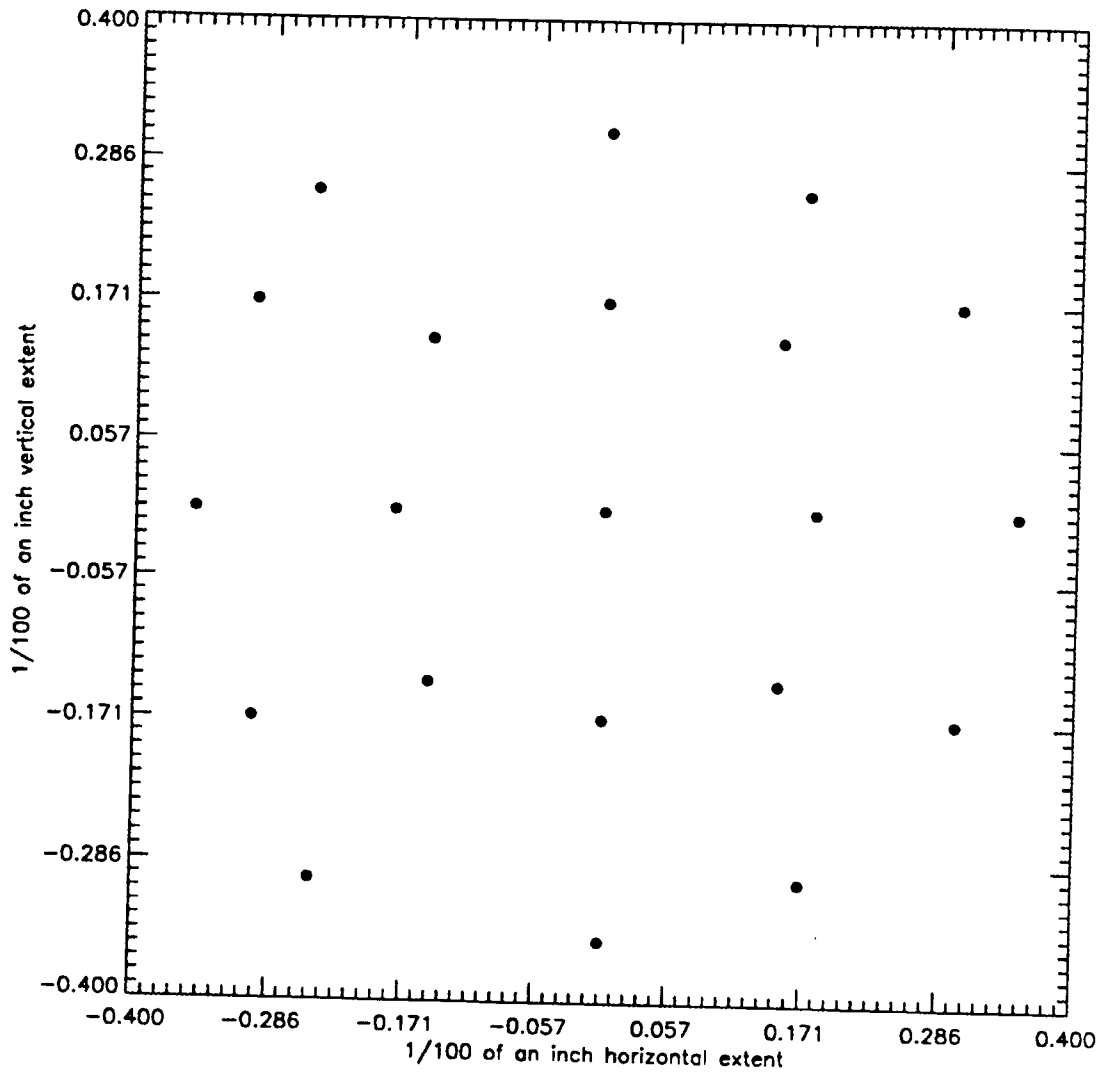Figure 18. Thickness contour for target shown in Figure 6.

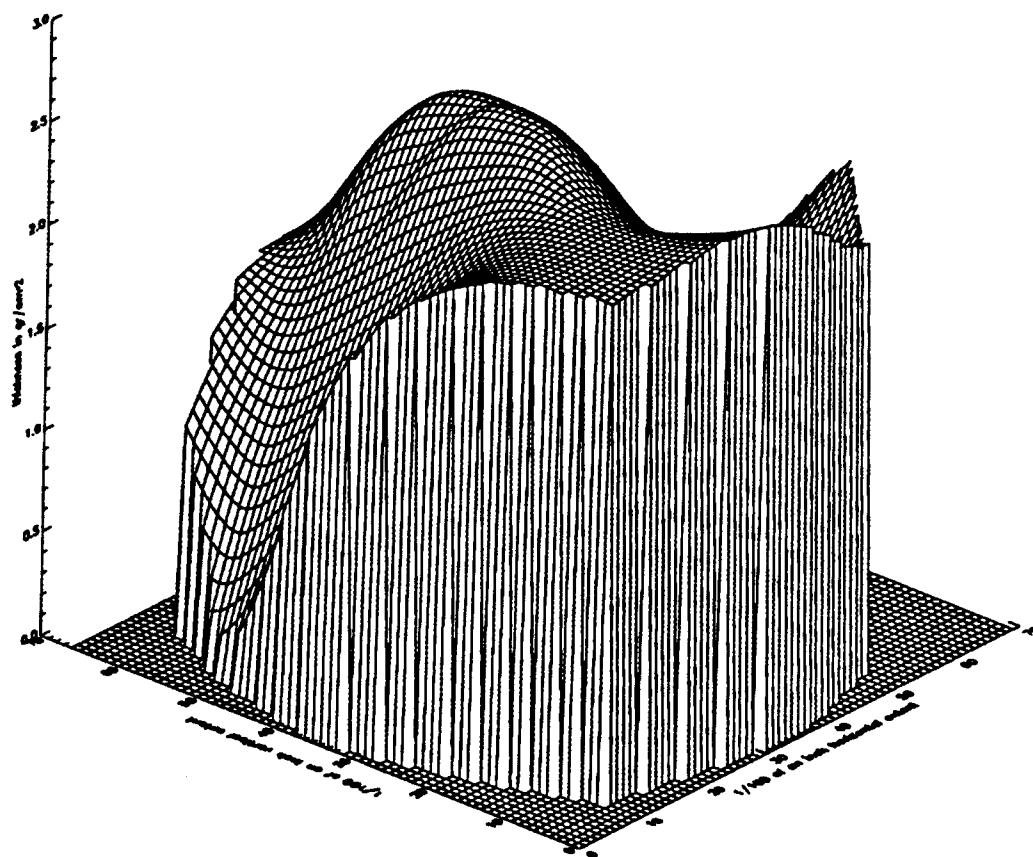Figure 19. Center of the "primed" scan points #'s 1-6, 7', 8, 9', 10-14, 15', 16, 17', 18-21.

32

Figure 20. Thickness variation for stick #3b prime, bottom, HEPL NH₃ target. Data presented in Table 9.
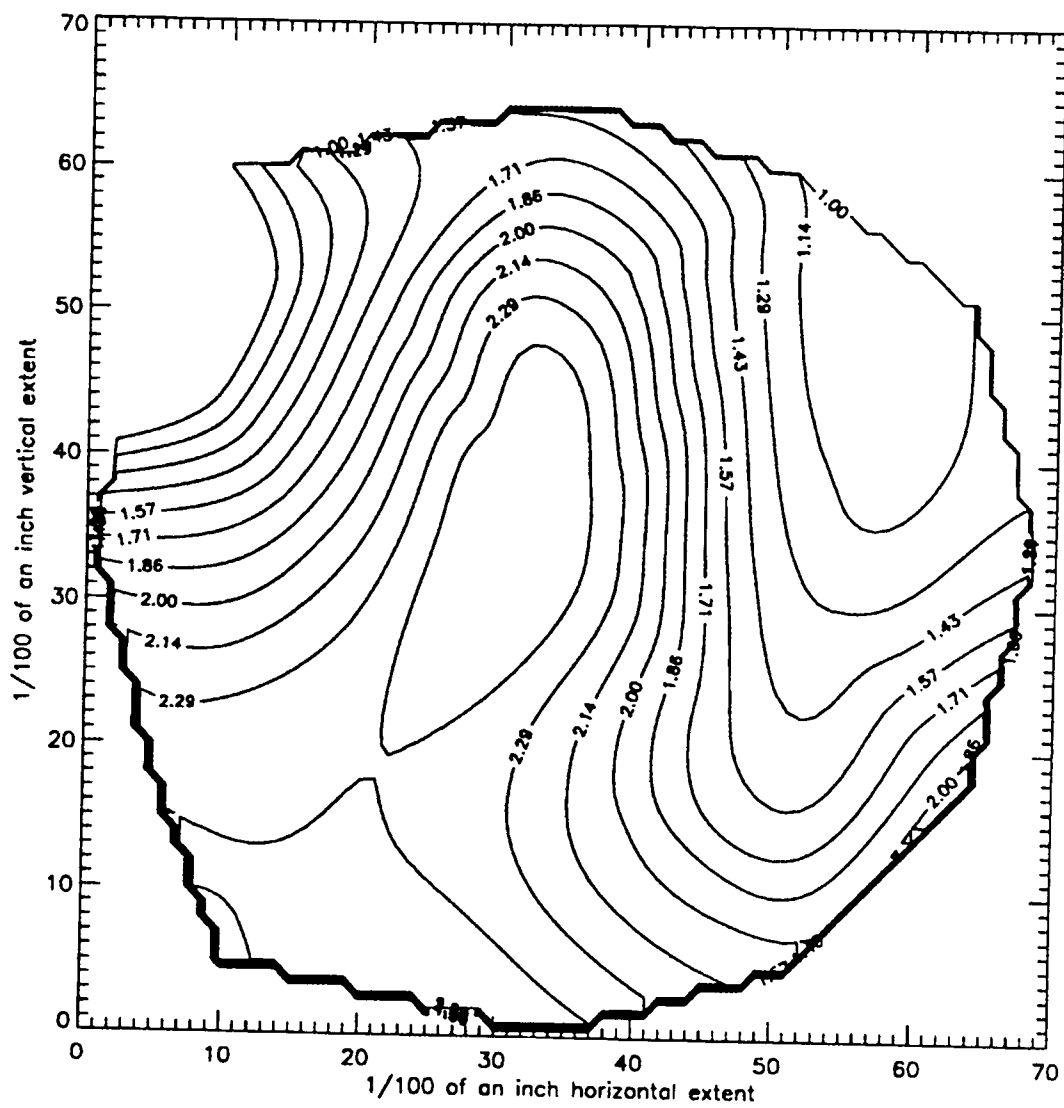
Figure 21. Thickness contour for target shown in Figure 9.

LIST OF REFERENCES

Abe, K., *et al.*, E143, SLAC-PUB-6508, Physical Review Letters preprint, August, 1994.

Adams, *et al.*, SMC, Physics Letters, B329, p. 399, 1994.

Adeva, B., *et al.*, SMC, Physics Letters, B302, p. 533, 1993.

AIC Software, 1993. Compiled from: Natl. Bureau of Standards (Berger and Hubbell, 1987), Los
    Alamos National Laboratory (Storm and Israel, 1967) and Kaman Sciences (Viegele et al., 1971).

Alguard, M.J., *et al.*, SLAC E80, Physical Review Letters, 37, p. 1261, 1976; 41 and 70, 1978..

Amaudruz, P., *et al.*, NMC, Physics Letters, B295, p. 159, 1992.

Anderson, H.J., *et al.*, Physics Vad Mecum 2nd Ed. , 1989.

Anthony, P.L., *et al.*, E142, Physical Review Letters, 71, p. 959, 1993.

Ashman, J., *et al.*, EMC, Physics Letters, B206, p. 364, 1988; Nuclear Physics, B328, p. 1, 1989.

Baum, G., *et al.*, E130, Physical Review Letters, p. 51, 1135, 1983.

Bjorken, J.D., Physical Review, 148, p. 1467, 1966; D1, p. 376, 1970.

Bjorken, J.D. and Paschos, E.A., Physical Review, 185, p. 1975, 1969.

Bosted, P., E143 Technical Note 19, 1993 and multiple e-mail, in person and phone conversations, 1994.

Canberra Nuclear Products Group, Meriden CT, product Catalog, 8th edition, 1989.

Crabb, D.G., *et al.*, Physical Review Letters, 64, p. 2627, 1990.

Drell, S.D., Levy, D.J. and Yan, T., Physical Review, 187, p. 2159, 1969.

Ellis, J. and Jaffe, R., Physical Review, D9, p. 1444, 1974; D10, p. 1669, 1974.

Feynman, R.P., Photon - Hadron Interactions, W.A. Benjamin, Inc., Reading, MA, 1972.

Hey, A.J.G. and Mandula, J.E.,Physical review, D5, p.2610, 1972.

Hughes, V.W. and Kuti, J., Annual Review of Nuclear and Particle Science, pp. 611-644, 1983.

Jaffe, R.L. and Ji, X., Physical Review, D43, p. 724, 1991.

Ji, X., Nuclear Physics, B402, pp. 217-250, 1993.

Kaku, M., Quantum Field Theory, Oxford University Press, New York, 1993.

Kuti, J. and Weisskopf, F., Physical Review, D4, p. 3418, 1971.

Stuart, L.M., "E143 target specifications summary" memo of 04 November, 1993.

McCarthy, J., *et al.*, SLAC (unpublished) E143 Collaboration Proposal, 1993.

McMaster, V., et al., UCRL-50174-Sec.1-Rev.1, 1967.

Microsoft Corp., "Excel," Version 4.0, Redmond, WA, 1993.

Oxford/Tennelec, "Nucleus PCA-II," Oak Ridge TN, 1990.

Pokorski, S., Gauge Field Theories, Cambridge University Press, London, 1987.

Rondon, O.A., UVA-INPP-PUB-91-15, 1991.

Taylor, J.R., An Introduction to Error Analysis, 1982, Oxford.

Williams, *et al.*, G. E. Chart of the Nuclides, 13th Ed., 1984.

INITIAL DISTRIBUTION LIST

1. Defense Technical Information Center...2
    Cameron Station
    Alexandria, VA 22304-6145

2. Library, Code 52...2
    Naval Postgraduate School
    Monterey, CA 93943-5101

3. Professor X.K. Maruyama..5
    Department of Physics, Code PH/Mx
    Naval Postgraduate School
    Monterey, CA 93943-5000

4. Professor F.R. Buskirk..2
    Department of Physics, Code PH/Bs
    Naval Postgraduate School
    Monterey, CA 93943-5000

5. LT D.R. Garvey (OZ Division Officer)...2
    U.S.S. Abraham Lincoln (CVN-72)
    FPO AP 96612-2872

6. Mr. E.W. Garvey..1
    P.O. Box 73216
    Puyallup, Washington 98373

7. Mr. R. Siegfried...1
    C/O Mountain View High School
    1500 S.E. Blairmont
    Vancouver, Washington 98684-8399